



# A set point in the selection of the $\alpha\beta$ TCR T cell repertoire imposed by pre-TCR signaling strength

Elena R. Bovolenta<sup>a</sup>, Eva M. García-Cuesta<sup>b</sup>, Lydia Horndler<sup>a</sup>, Julia Ponomarenko<sup>c,d</sup>, Wolfgang W. Schamel<sup>e,f,g,h</sup>, Mario Mellado<sup>b</sup>, Mario Castro<sup>i</sup>, David Abial<sup>i</sup>, and Hisse M. van Santen<sup>a,1</sup>

Edited by Christophe Benoist, Harvard Medical School, Boston, MA; received February 2, 2022; accepted April 19, 2022

Signaling via the T cell receptor (TCR) is critical during the development, maintenance, and activation of T cells. Quantitative aspects of TCR signaling have an important role during positive and negative selection, lineage choice, and ability to respond to small amounts of antigen. By using a mutant mouse line expressing a hypomorphic allele of the CD3 $\zeta$  chain, we show here that the strength of pre-TCR-mediated signaling during T cell development determines the diversity of the TCR $\beta$  repertoire available for positive and negative selection, and hence of the final  $\alpha\beta$ TCR repertoire. This finding uncovers an unexpected, pre-TCR signaling-dependent and repertoire-shaping role for  $\beta$ -selection beyond selection of in-frame rearranged TCR $\beta$  chains. Our data furthermore support a model of pre-TCR signaling in which the arrangement of this receptor in stable nanoclusters determines its quantitative signaling capacity.

pre-TCR | signaling | diversity | repertoire |  $\beta$ -selection

Signaling via the T cell receptor (TCR) is induced upon its interaction with cognate peptide-major histocompatibility complex (pMHC) ligands. The TCR has low affinity for pMHC (1–3), but is able to cause the activation and response of the mature T cell upon exquisitely specific recognition of a small number of these pMHC ligands on professional antigen-presenting cells (APCs) or target cells (4–6). The molecular mechanisms that resolve the apparent contradiction between low affinity, specificity, and high sensitivity are of interest because of the crucial role of TCR-mediated signaling in guaranteeing protective immunity and homeostasis. Their understanding can identify targets that can be used to control the immune response in therapeutic settings. In previous work, we and others identified one of these mechanisms, showing that the TCR organizes itself in nanoclusters at the T cell surface, already before antigenic stimulation, and presenting evidence that these TCR nanoclusters provide the T cell with enhanced sensitivity for its pMHC ligands (7–9). Furthermore, we could show that, concomitant with their differentiation from a naïve into a memory state, T cells increase sensitivity for their cognate ligand by enrichment for TCR nanoclusters (8–10). However, we have very little insight into the relevance of this mechanism during the stepwise developmental process that results in the generation of MHC-restricted self-tolerant mature T cells. Such knowledge is important, given that modulation of TCR signaling strength at particular T cell developmental stages determines the makeup and functional capacity of the mature T cell repertoire (11–13).

We previously demonstrated that the mutation of a single amino acid in the transmembrane domain of the TCR-associated CD3 $\zeta$  chain impairs the formation of TCR nanoclusters and affects the TCR sensitivity of mature T cells (8). Based on this finding, we have generated a mutant mouse model to address the role of TCR nanocluster formation and T cell sensitivity in an organismal setting. We present an analysis of the successive T cell developmental stages in such mice, and show that the mutation impairs the maturation of T cell progenitors with in-frame rearranged TCR $\beta$  genes, at one of the earliest T cell developmental checkpoints, which is dependent on signaling through the pre-TCR. The mutation converts CD3 $\zeta$  into a hypomorphic mutant that reduces intrinsic and downstream signaling capacity of the pre-TCR, suggesting an important role for pre-TCR nanoclustering in its function. Using a next-generation sequencing approach, we furthermore provide direct evidence for an important role of pre-TCR signaling intensity in shaping the diversity of the TCR $\beta$  repertoire.

## Results

**L19A Mice Have a Defect in Early Thymic  $\alpha\beta$ T Cell Differentiation.** We previously showed that a leucine-to-alanine mutation at position 19 (L19A) of the murine CD3 $\zeta$  transmembrane domain reduced TCR nanoclustering, concomitant with a decrease in

## Significance

The ability of the T cell receptor (TCR) to convey signals of different intensity is essential for the generation of a diverse, protecting, and self-tolerant T cell repertoire. We provide evidence that pre-TCR signaling during the first stage of T cell differentiation, thought to only check for in-frame rearrangement of TCR $\beta$  gene segments, determines the degree of diversity in a signaling intensity-dependent manner and controls the diversity of the TCR repertoire available for subsequent thymic positive and negative selection. Pre-TCR signaling intensity is regulated by the transmembrane region of its associated CD3 $\zeta$  chains, possibly by organizing pre-TCRs into nanoclusters. Our data provide insights into immune receptor signaling mechanisms and reveal an additional checkpoint of T cell repertoire diversity.

Author contributions: E.R.B., E.M.G.-C., W.W.S., M.M., and H.M.v.S. designed research; E.R.B., E.M.G.-C., L.H., and H.M.v.S. performed research; J.P., M.C., and D.A. contributed new reagents/analytic tools; E.R.B., E.M.G.-C., L.H., J.P., W.W.S., M.M., M.C., D.A., and H.M.v.S. analyzed data; E.R.B. and H.M.v.S. wrote the paper; and W.W.S., M.C., and H.M.v.S. acquired funding.

The authors declare no competing interest.

This article is a PNAS Direct Submission.

Copyright © 2022 the Author(s). Published by PNAS. This article is distributed under [Creative Commons Attribution-NonCommercial-NoDerivatives License 4.0 \(CC BY-NC-ND\)](https://creativecommons.org/licenses/by-nc-nd/4.0/).

<sup>1</sup>To whom correspondence may be addressed. Email: hvansanten@cbm.csic.es.

This article contains supporting information online at <http://www.pnas.org/lookup/suppl/doi:10.1073/pnas.2201907119/-DCSupplemental>.

Published May 26, 2022.

T cell sensitivity (8). We generated transgenic mice expressing wild-type (WT) or L19A CD3 $\zeta$ -GFP (green fluorescent protein) fusion proteins under control of the hCD2 promoter and enhancer-regulated transgene cassette (14) and backcrossed these mice to a *Cd3z*<sup>-/-</sup> background (15) so that the GFP-CD3 $\zeta$  chains were the only CD3 $\zeta$  chains expressed in these mice. Immunoblot analysis of whole lysates from total thymus and purified double-negative (DN) thymocytes showed the presence of ~100-kDa covalently associated homodimers reactive with both CD3 $\zeta$ - and GFP-specific antibodies (*SI Appendix, Fig. S1 A and B*). Homogeneous expression of the transgenic CD3 $\zeta$ -GFP fusion proteins was detected by flow cytometry in all thymic subsets tested (*SI Appendix, Fig. S1 C*). Mice on this background will be referred to as WT and L19A mice. We pooled the data of the two independent lines analyzed of each genotype, as we did not observe phenotypic differences between them (*SI Appendix, Fig. S1 D*).

Thymi isolated from L19A mice contained two- to threefold fewer cells than thymi from WT mice (Fig. 1 *A, Upper*). The double-positive (DP), 4SP, and 8SP populations were reduced in number whereas there was a relative increase in DN

thymocytes, indicating a defect in thymocyte differentiation that was occurring at the DN stage in L19A mice (Fig. 1 *A, Middle and Lower*). Subdivision of the DN population into the DN1 to DN4 subsets using the CD25 and CD44 markers (16) revealed similar percentages and numbers of CD44<sup>+</sup>CD25<sup>-</sup> DN1 and CD44<sup>+</sup>CD25<sup>+</sup> DN2 cells in L19A and WT thymi but a relative accumulation of CD44<sup>-</sup>CD25<sup>+</sup> DN3 cells and a relative and absolute reduction of CD44<sup>-</sup>CD25<sup>-</sup> DN4 cells in L19A thymi as compared with WT thymi (Fig. 1 *B*). Thus, the earliest observable defect in  $\alpha\beta$ T cell differentiation in L19A mice occurred at the transition from the DN3 to DN4 stage. The absolute numbers of DN4 thymocytes and the percentages of DN3 and DN4 mutant thymocytes were significantly different from those of CD3 $\zeta$ -deficient mice (Fig. 1 *B*), which present an almost complete loss of the DN4 population, indicating that the L19A CD3 $\zeta$  chain could at least partially overcome defects imposed by *Cd3z* deficiency on pre-TCR function.

The DN3-to-DN4 transition depends on the formation and function of the pre-TCR, a CD3-associated heterodimer of an in-frame rearranged TCR $\beta$  chain and an invariant pT $\alpha$  chain (17). DN3 thymocytes that have rearranged the TCR $\beta$  chain

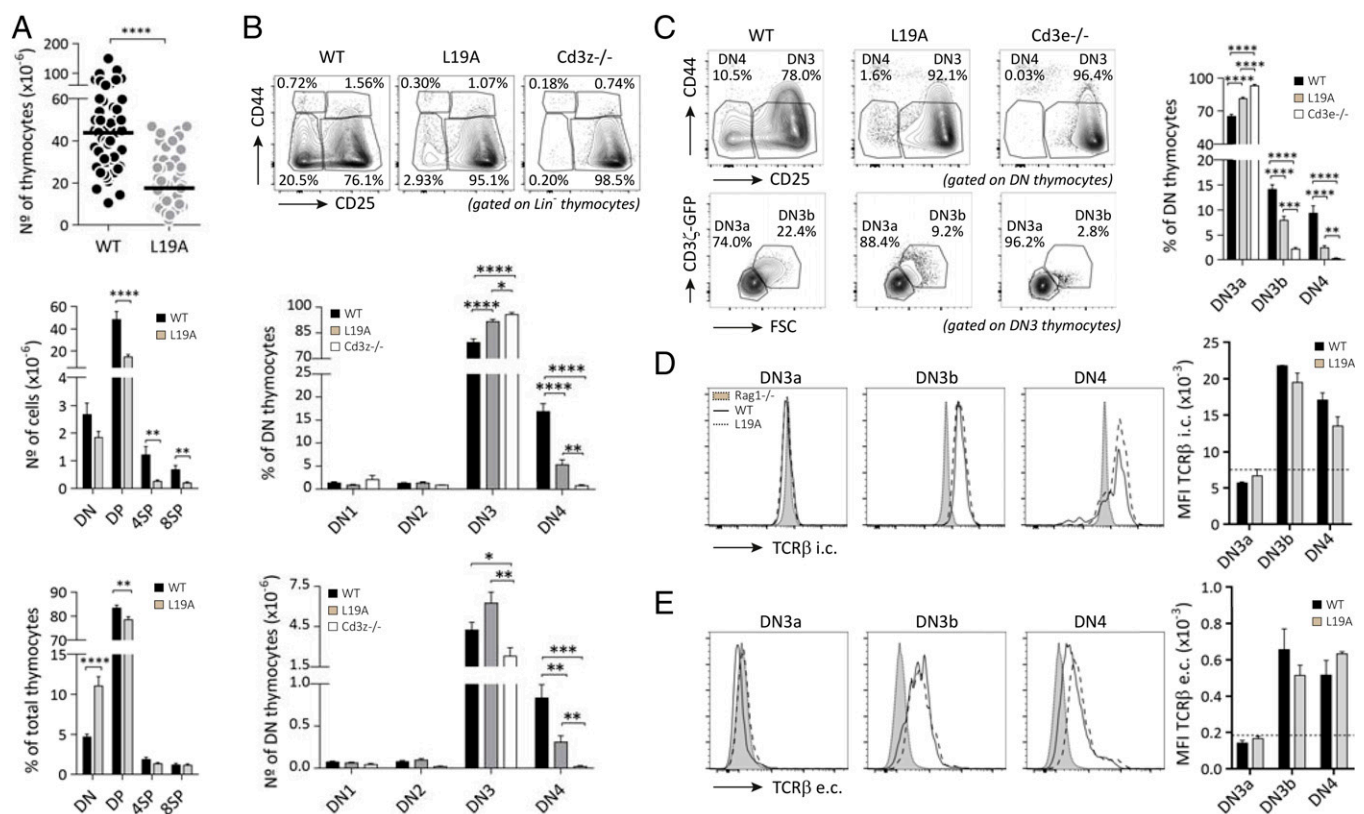


**Fig. 1.** Reduction in size of thymic populations and impaired DN3a-to-DN3b transition in L19A mice. (A) Quantification of the total number of thymocytes (*Upper*). Each dot shows the total number of thymocytes in an individual mouse. Quantification of the number (*Middle*) and percentage (*Lower*) of thymocytes in the major populations defined according to expression of CD4 and CD8. Results and statistical analysis shown are based on pooled data from 67 WT and 72 L19A mice from 10 independent experiments. (B) Representative plots of the DN (CD4<sup>-</sup>CD8<sup>-</sup>) subpopulations defined by the expression of CD44 and CD25 (*Upper*) and quantification of the percentage (*Middle*) and cell number (*Lower*) of these populations in WT, L19A, and *Cd3z*<sup>-/-</sup> mice. The DN population was pregated on the lineage negative (Lin<sup>-</sup>) population (CD4<sup>-</sup>, CD8<sup>-</sup>, CD19<sup>-</sup>, B220<sup>-</sup>, GR1<sup>-</sup>, NK1.1<sup>-</sup>, TCR $\gamma\delta$ <sup>-</sup>, CD11b<sup>-</sup>, CD11c<sup>-</sup>, TER119<sup>-</sup>). IEL precursors, identified as Lin<sup>-</sup>CD24<sup>lo</sup>CD5<sup>hi</sup>TCR $\beta$ <sup>hi</sup>CD44<sup>lo</sup> cells, were excluded from the quantifications. Graphs show the averages calculated on the basis of data obtained from three independent experiments with 12 WT, 12 L19A, and 5 *Cd3z*<sup>-/-</sup> mice. (C) Representative flow cytometry plots of Lin<sup>-</sup> DN populations (defined as above) in WT, L19A, and *Cd3e*<sup>-/-</sup> thymi according to CD44 and CD25 markers (*Upper*; CD25<sup>+</sup>CD44<sup>-</sup> DN3 and CD25<sup>-</sup>CD44<sup>-</sup> DN4 gates indicated) and identification of DN3a and DN3b subpopulations within the DN3 gate according to forward scatter (FSC) and CD3 $\zeta$ -GFP expression (*Lower*). (C, *Right*) Quantification based on pooled data from six independent experiments showing the percentage of the DN3a, DN3b, and DN4 populations. (D) Representative histograms (*Left*) and quantification (*Right*) of the intracellular TCR $\beta$  expression levels in the DN3a (CD44<sup>+</sup>CD25<sup>+</sup>), DN3b (CD44<sup>+</sup>CD25<sup>+</sup>), and DN4 (CD44<sup>+</sup>CD25<sup>-</sup>) subpopulations. Thymocytes from *Rag1*-deficient mice were used as a control for intracellular staining and used as background control in all three overlays. Dashed lines indicate signal intensity obtained in *Rag1*<sup>-/-</sup> thymocytes. Quantification for one out of four experiments is shown. (E) Representative histograms (*Left*) and quantification (*Right*) of extracellular TCR $\beta$  expression. Data represent quantification for one out of four experiments. All quantifications are presented as the mean  $\pm$  SEM. *P* values were calculated using unpaired two-tailed Student's *t* tests with 95% CI (\**P* < 0.05, \*\**P* < 0.01, \*\*\**P* < 0.001, \*\*\*\**P* < 0.0001). e.c., extracellular; i.c., intracellular.

(DN3b thymocytes) can be distinguished from their immediate precursors (DN3a thymocytes) by phenotypical changes induced upon pre-TCR signaling, including an increase in cell size (18). Applying this criterion, we quantified the percentage of DN3a and DN3b thymocytes in the DN population of L19A and WT mice using as a reference DN3 thymocytes from *Cd3e*-deficient mice, which can rearrange their *Tcrb* locus but cannot express the pre-TCR and do not reach the DN3b stage (19). L19A thymi contained significantly more DN3a and fewer DN3b thymocytes than WT thymi (Fig. 1C). This lag in T cell development was not due to the inability of L19A thymocytes to rearrange their *Tcrb* locus, as intracellular staining for TCR $\beta$  in the DN3b and DN4 populations of WT and L19A thymi showed an equal intensity (Fig. 1D). Moreover, cell-surface expression of the pre-TCR on the DN3b-enriched CD44<sup>+</sup>CD25<sup>lo</sup> population and CD44<sup>+</sup>CD25<sup>+</sup> DN4 cells, measured by extracellular staining with an antibody against the TCR $\beta$  chain, was indistinguishable between L19A and WT mice (Fig. 1E). Likewise, cell-surface expression of CD3 $\epsilon$  and pT $\alpha$  and expression of the transgenic CD3 $\zeta$ -GFP chain were equal for WT and L19A DN3b and DN4 thymocytes (SI Appendix, Fig. S2 A–D). We found that cell-surface expression and stoichiometry of the cell surface–displayed complexes of the pre-TCR were not affected by the L19A mutation in cell lines derived from the pre-T cell line SCB.29 (20), rendered *Cd3z*-deficient via CRISPR-Cas9-mediated gene editing, and reconstituted with WT or L19A CD3 $\zeta$ -GFP (SI Appendix, Fig. S3 A–C). Immunoprecipitation experiments of the pre-TCR in these cell lines showed that the ratio of CD3 $\zeta$  over CD3 $\epsilon$  in immunoprecipitates with TCR $\beta$ - and CD3 $\epsilon$ -specific antibodies was lower in the L19A cell lines than in WT cell lines, suggesting that under these conditions the association between CD3 $\zeta$  and the other components of the pre-TCR was weaker (SI Appendix, Fig. S3D).

### The L19A Mutation Impairs Pre-TCR Signaling and Function.

Signaling via the pre-TCR promotes the survival and proliferation of DN3 thymocytes with an in-frame rearranged *Tcrb* locus and permits their differentiation to the DP stage in a process termed “ $\beta$ -selection” (21). In order to capture the physiological signaling status of pre-TCR in WT and L19A thymocytes, we determined the activation level of pre-TCR signaling pathway components directly ex vivo, without stimulation with anti-CD3 or -TCR $\beta$  antibodies. We first focused on the proline-rich sequence (PRS) of the intracellular domain of CD3 $\epsilon$ , which is known to be selectively exposed in active TCRs and can be detected by intracellular staining with the APA1/1 monoclonal antibody (mAb) (22, 23). We used DN thymocytes from knockin PRS (KIPRS) mice as a negative control for staining, as the key proline residues in the CD3 $\epsilon$  PRS of these mice are mutated to alanine, abrogating recognition by the APA1/1 mAb (24). Freshly isolated DN3b and DN4 thymocytes from WT and L19A mice, identified as CD44<sup>+</sup>CD25<sup>lo</sup> and CD44<sup>+</sup>CD25<sup>+</sup> DN thymocytes, respectively, showed specific staining (Fig. 2A). However, L19A DN3b and DN4 thymocytes showed a significantly lower APA1/1 staining intensity than WT DN3b and DN4 thymocytes, consistent with reduced pre-TCR signaling. This was not due to a lower expression level of CD3 $\epsilon$  in L19A thymocytes (SI Appendix, Fig. S2C) but indicated fewer active pre-TCRs in L19A thymocytes. The high and equal level of APA1/1 staining observed in WT and L19A DN3a thymocytes was expected, as in the absence of TCR $\beta$  the CD3 $\epsilon$  chains are retained in the endoplasmic reticulum and are in the conformation recognized by the APA1/1 mAb (25). We also measured phosphorylation of the receptor-proximal signaling molecule ZAP70 in freshly isolated thymocytes, including

treatment with the Lck inhibitor A770041 as a specificity control. L19A DN3b and DN4 thymocytes showed decreased phosphorylation of Y319 of ZAP70 as compared with WT thymocytes (Fig. 2B). No such differences were found in DN3a thymocytes. We extended these data using the WT and L19A pre-T cell lines. Steady-state CD3 $\epsilon$  immunoreceptor tyrosine-based activation motif (ITAM) phosphorylation was decreased in the L19A cell lines as compared with the WT cell lines (SI Appendix, Fig. S4A). Upon stimulation of these cell lines with a CD3 $\epsilon$ -specific antibody, we observed decreased CD3 $\zeta$  and ZAP70 phosphorylation in L19A cell lines as compared with WT cell lines (SI Appendix, Fig. S4 B and C). We measured the functional consequences of this impaired signaling, focusing on induction of markers associated with differentiation, proliferation, and survival. Up-regulation of the transferrin receptor (CD71; Fig. 2C) and the large neutral amino acid transporter subunit CD98 (Fig. 2D) was significantly impaired in DN3b and particularly in DN4 thymocytes of L19A mice. CD25 cell-surface expression, down-regulation of which is reduced in mice with defects in pre-TCR components and associated signaling molecules (26, 27) and is considered a marker for pre-TCR signal intensity received by DN cells, was higher in L19A DN3 thymocytes than in WT DN3 thymocytes (Fig. 2E). Bromodeoxyuridine (BrdU)-positive, proliferating DN3 and DN4 L19A thymocytes were clearly diminished in numbers as compared with the corresponding WT thymocytes (Fig. 2F) and L19A thymocytes were also more prone to undergo apoptosis than WT thymocytes (Fig. 2G). These results clearly indicated that the function of the pre-TCR in L19A mice was impaired, providing an explanation for the observed differentiation defect.

### CD3 $\zeta$ Regulates the Motion and Cell-Surface Organization of the Pre-TCR.

Most available data support the concept that the pre-TCR signals in the absence of ligands and pre-TCR dimers have been proposed as the unit of signaling (28). Given our previous findings on the effect of the L19A mutation on TCR organization, we assessed the distribution of the pre-TCR at the cell surface of WT and L19A thymocytes. We purified DN3 and DN4 thymocytes excluding the 1% GFP-brightest cells that were not amenable to individual particle observation, adhered them to fibronectin-coated coverslips, and analyzed them via total internal reflection fluorescence (TIRF) microscopy (Fig. 3A). We used the CD3 $\zeta$ -coupled GFP as the label to track the pre-TCR complexes, as cell-surface labeling of WT and L19A DN thymocytes showed a strong correlation between GFP signal and CD3 $\epsilon$  staining (SI Appendix, Fig. S2E). Only fluorescent particles that were continuously detectable and did not fuse or split during a time period of at least 5 s were analyzed. The average number of particles detected at the cell surface of L19A DN thymocytes was significantly lower than observed for WT DN thymocytes (Fig. 3B), even though no difference in the total level of expression of pre-TCRs was observed for these populations (Fig. 1E and SI Appendix, Fig. S2 A–D). L19A pre-TCR particles had an increased diffusion rate as compared with WT particles (Fig. 3C). There was no significant difference in distribution between confined, free, and directed diffusion of mobile particles (Fig. 3D) excluding a shift in diffusion mode as the mechanism underlying the overall speed-up. Particles displayed a wide range of fluorescence intensities, suggesting that pre-TCRs grouped in clusters of various sizes (Fig. 3E). However, L19A particles displayed a lower average intensity than WT particles, with a marked underrepresentation of higher-intensity particles. These data are compatible with the notion that WT pre-TCRs form stable nanoclusters and that the L19A mutation reduces their size.



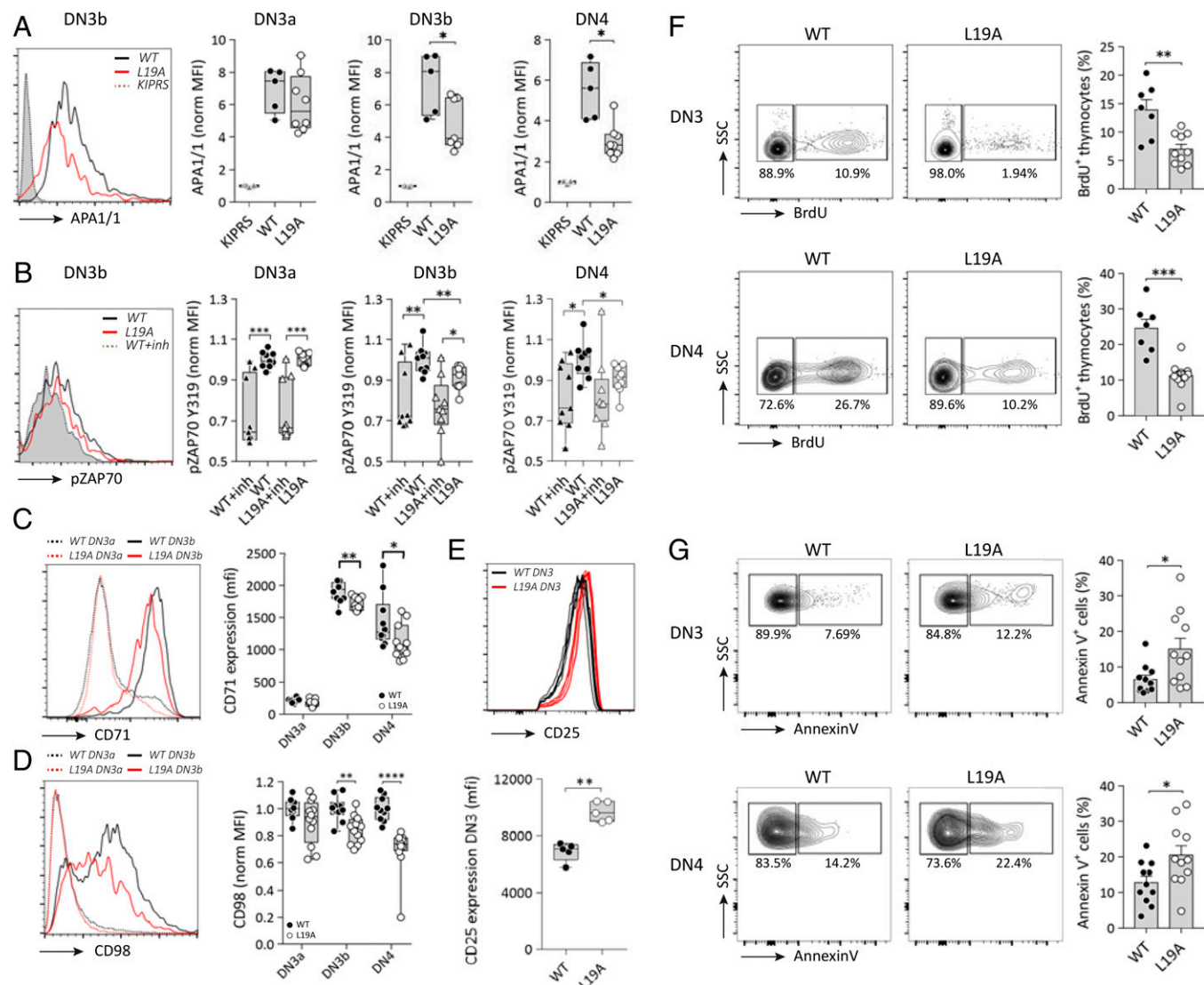


**Fig. 2.** CD3 $\zeta$  transmembrane region regulates pre-TCR-dependent signaling and function. (A) Representative histogram of intracellular APA1/1 staining in DN3b thymocytes and box and whisker plots depicting normalized quantification of staining in DN3a, DN3b, and DN4 subsets of pooled data from two independent experiments. Boxes show the median and extend from the 25th to 75th percentile. Whiskers reach up and down to the largest and smallest value, respectively, and individual data points are indicated by symbols. (B) Representative histograms and normalized quantification of intracellular pZAP70 (P-Y319) labeling. Box and whisker plots are as in A. (C and D) Representative histograms and quantification of expression of the CD71 (C) and CD98 (D) maturation markers at the cell surface of DN3a, DN3b, and DN4 thymocytes. CD44<sup>+</sup> DN subsets were gated according to CD25 levels: DN3a (CD25<sup>hi</sup>), DN3b (CD25<sup>lo</sup>), and DN4 (CD25<sup>+</sup>). Box and whisker plots (as in A) present normalized quantification of pooled data from four independent experiments. (E) CD25 expression on DN3 (CD25<sup>+/lo</sup>CD44<sup>+</sup>) thymocytes of WT and L19A mice. Overlay of staining profiles (Upper) and quantification (Lower) for one out of seven experiments quantified are shown. (F) Representative plots of BrdU staining in DN3 and DN4 populations and quantification of the percentage of BrdU<sup>+</sup> thymocytes in each population. Thymocytes shown in the plots were pregated on the Lin<sup>+</sup>CD44<sup>+</sup> population. Graphs present the mean  $\pm$  SEM of pooled data from three independent experiments. SSC, side scatter. (G) Representative plots and quantification of Annexin V binding in the indicated populations. Thymocytes shown in the plots were pregated on the Lin<sup>+</sup>CD44<sup>+</sup> population. Quantification shows the mean  $\pm$  SEM of pooled data from four independent experiments. P values were calculated using unpaired two-tailed Student's *t* tests with 95% CI (\**P* < 0.05, \*\**P* < 0.01, \*\*\**P* < 0.001, \*\*\*\**P* < 0.0001).

### TCR $\beta$ Repertoire Diversity Is Regulated by the Intensity of Pre-TCR Signaling.

In order to determine whether the intensity of pre-TCR signaling has a functional impact on the  $\beta$ -selected TCR $\beta$  repertoire, we assessed TCR $\beta$  diversity in post- $\beta$ -selection, large CD69<sup>+</sup> DP WT and L19A thymocytes, which have not yet been subjected to negative and positive selection (Fig. 4A). We determined the V, D, J, and CDR3 identity of each TCR $\beta$  chain by amplifying their complementary DNAs (cDNAs) via an unbiased 5' rapid amplification of cDNA ends (RACE) protocol and high-throughput amplicon sequencing. Both the number of recovered cells and in-frame reads obtained from them were higher for WT than L19A thymi (Table 1). This was in line with the finding that WT cells produced more early DP thymocytes (SI Appendix, Fig. S5A). We determined the effective number of

clones in each repertoire by calculating Hill numbers  $^qD$  via rarefaction and extrapolation methods (29), with  $^0D$  the effective number of different clones. Rarefaction curves for the WT DP repertoires separated almost completely from the curves for L19A DP repertoires (Fig. 4B) and the observed and estimated numbers of clones were significantly higher in WT than L19A DP repertoires (Table 1), indicating that TCR $\beta$  repertoires were more diverse in WT mice than in L19A mice. Calculating diversity using *q* values of 1 and 2, thereby providing more weight to the more abundant clones within the populations, gave an essentially identical pattern of diversities (SI Appendix, Fig. S5B and C). The latter provided evidence for the robustness of the analysis of early DP repertoire diversity. The coverage (29) for each mouse was above 0.98 so the extrapolated parts of the curve were close

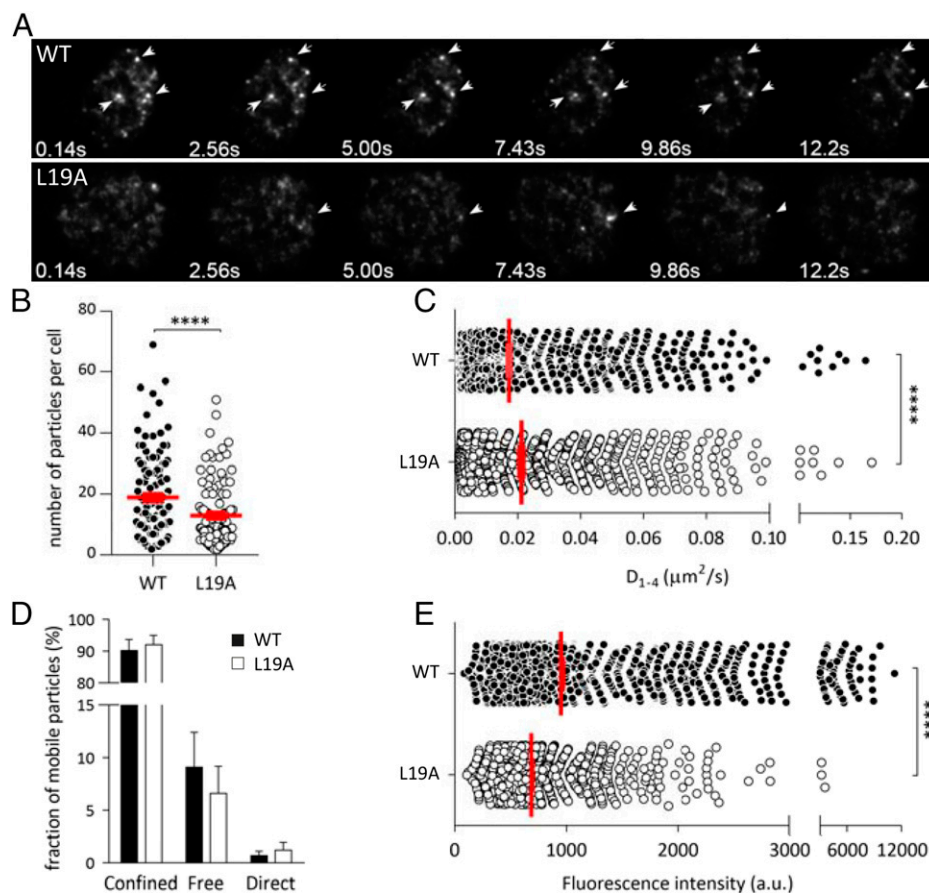


**Fig. 3.** TIRF microscopy analysis of the pre-TCR on CD44<sup>-</sup> DN primary thymocytes. (A) Representative time-lapse images of WT and L19A CD44<sup>-</sup> DN thymocytes. Arrowheads identify individual particles on a WT (3 particles) and a L19A (1 particle) thymocyte at the indicated time points. (B) Number of stable fluorescent particles detected on WT and L19A thymocytes; horizontal bars indicate mean particle number for each genotype. (C) Short-time-lag diffusion coefficient ( $D_{1-4}$ ) of the mobile particles detected in the analysis. Means  $\pm$  SEM are indicated by red lines. (D) Quantification of the percentage (mean  $\pm$  SEM) of mobile particles for confined, free, and directed diffusion tracks. (E) MFI of mobile particles during the first 20 frames in which the particles are visible. Each dot in the graph presents a single CD3 $\zeta$ -GFP spot. Means  $\pm$  SEM are indicated by red lines. Pooled data were obtained in four independent experiments encompassing 131 WT cells (range 20 to 57 cells per experiment) and 110 L19A cells (range 13 to 40 cells per experiment).  $P$  values were calculated using an unpaired two-tailed Student's  $t$  test with 95% CI (\*\*\* $P$  < 0.001, \*\*\*\* $P$  < 0.0001). a.u., arbitrary units.

to the asymptotic diversity and guaranteed that the estimation of the diversity of the repertoires was accurate (SI Appendix, Fig. S5D). Furthermore, we addressed the effect of sample size on diversity estimates and found that this was not a confounding factor in the approaches we used (SI Appendix, Text S1). We also compared diversity of the TCR $\beta$  repertoire in WT and L19A CD25<sup>hi</sup>CD44<sup>-</sup> DN3 thymocytes that contain cells that have rearranged the *Tcrb* gene segments but should have undergone little or no pre-TCR-mediated selection and expansion (Fig. 4A). There were no significant differences in the number of recovered cells or in the number of in-frame reads (Table 1). No clear separation of rarefaction curves derived from the WT and L19A DN3 repertoires was observed (Fig. 4C) and the observed and estimated numbers of clones in WT and L19A DN repertoires were not significantly different (Table 1). Collectively, these findings underscored that the difference in repertoire diversity at the early DP stage was a consequence of reduced signaling by the pre-TCR during  $\beta$ -selection.

## Discussion

The role of pre-TCR signaling intensity in the transition from the DN3 to the DN4 and early DP stages and its consequences for the repertoire of thymocytes that can undergo positive and negative selection have barely been addressed. We demonstrate in primary murine DN thymocytes and pre-T cell lines that

the L19A mutation reduces steady-state and antibody-induced activation levels of signaling components within and downstream of the pre-TCR. We provide direct evidence that the reduced intensity of pre-TCR signaling in L19A mice has a quantitative impact on the TCR $\beta$  diversity of the population of early DP thymocytes that still need to undergo positive and negative selection. This latter finding implies that during  $\beta$ -selection not all DN precursors with in-frame rearranged *Tcrb* genes mature but that pre-TCR signaling efficiency imposes a filter on the emerging repertoire. Our data are compatible with a mechanism in which pre-TCR signaling intensity is regulated by nanoclusters of the pre-TCR.

We explain our findings via a model in which pre-TCR signaling intensity determines the likelihood that a DN thymocyte reaches the early DP stage. Continuous signaling would be necessary to maintain both proliferation and survival programs active during this transition, with lower intensities of signaling increasing the likelihood that a clone will die out. Within the context of the L19A mutation, we favor the interpretation that the L19A mutation interferes with the organization of the pre-TCR, reducing the number and size of nanoclusters displayed at the cell surface and thereby the signaling capacity of the pre-TCR, with a potentially weaker association of the L19A CD3 $\zeta$  chain with the rest of the pre-TCR complex representing an alternative mechanism per se or an integral part of the mechanism underlying the reduction in nanocluster formation. Our

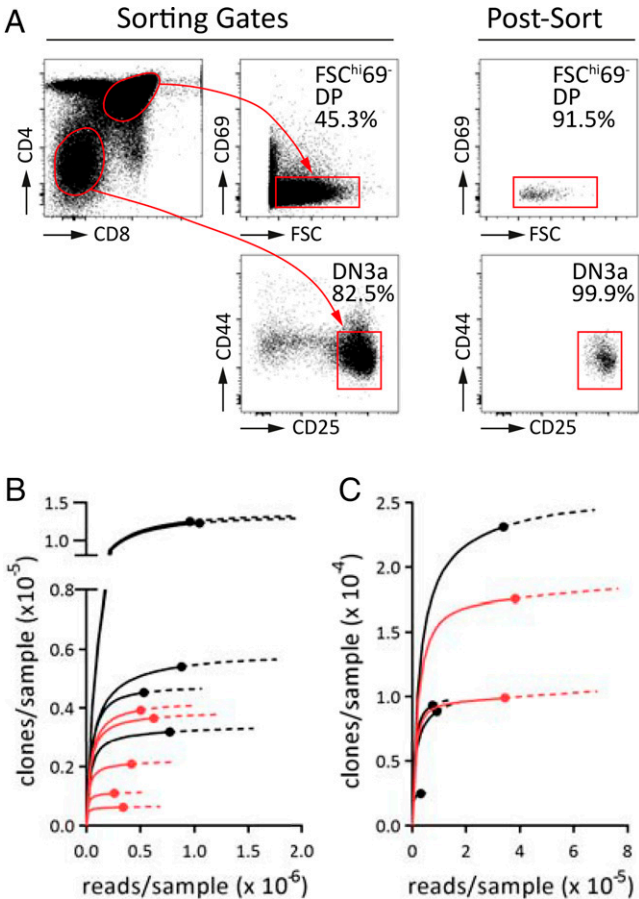


**Fig. 4.** TCR $\beta$  diversity of early DP and DN thymocytes in WT and L19A mice. (A) Sorting strategy for isolation of early DP and DN3 thymocytes. (B) Number of clones per sample estimated with the richness diversity ( $^0D$ ) for early DP thymocytes. Solid lines: rarefaction (interpolation) curves; dashed lines: extrapolation curves; symbols: observed diversity. Note that the observed values are, in all cases, close to the asymptotic part of the curves, consistent with the large values of the coverage (SI Appendix, Fig. S3C). (C) Number of clones per sample estimated for DN3 thymocytes. Meaning of lines and symbols is as in B.

previous work on the TCR has shown that nanoclusters provide increased antigen sensitivity to T cells (7), likely via cooperative signaling mechanisms within such clusters (30), and that the degree of organization of TCRs into nanoclusters scales with antigen sensitivity of the T cell (8). In the absence of at least canonical interactions with pMHC ligands (31), regulation of pre-TCR signaling would be expected to rely on pre-TCR intrinsic mechanisms. The most membrane-proximal pre-TCR signaling event that we found impaired in L19A DN3b and DN4 thymocytes is the conformational change that exposes the intracellular PRS of CD3 $\epsilon$  (32). The conformational change is

critical for pre-TCR-dependent signaling as  $\beta$ -selection is severely impaired in mice with mutations in the extracellular stalk domain of CD3 $\epsilon$  that abrogate this conformational change (23, 33) and in mice with a mutated or deleted PRS (24, 34). This event correlates in mature T cells with dislodging of the CD3 $\epsilon$  intracellular domain from the inner membrane leaflet, facilitating its recognition by the TCR-associated signaling machinery (35, 36), and is induced and maintained by ligand binding (37). The recent finding of direct binding of Lck to CD3 $\epsilon$  that depends on the conformational change (38) provides a mechanism in which a key initiator of pre-TCR signaling is recruited in a graded fashion to this complex as a function of the degree of conformational change. Our data support the notion that the fraction of pre-TCRs undergoing a conformational change depends on the degree of their organization in nanoclusters. The known role of the CD3 $\zeta$  transmembrane domain in TCR nanoclustering (8) and the here-reported correlation between signaling capacity and mobility and fluorescence intensity of pre-TCR particles in WT and L19A thymocytes make this a likely mechanism. Assuming that the pre-TCR oscillates between a signaling-competent, CD3 $\epsilon$ -exposing stage and a noncompetent stage, as has been proposed for the TCR (39, 40), we speculate that this exposure is stabilized by its interaction with neighboring pre-TCR complexes within pre-TCR nanoclusters. This interaction could in part rely on the inherent ability of the pT $\alpha$  extracellular domain to form homodimers, but would need the transmembrane domain of CD3 $\zeta$ . The range of fluorescence intensities that we observe in the WT thymocytes and their stability over time support the existence of nanoclusters bigger than the so far proposed pre-TCR dimers (41, 42). The limits of resolution of TIRF microscopy do not allow us to distinguish between the possibility that the observed particles represent pre-TCR nanoclusters of various sizes or whether these are stable membrane domains that contain more or fewer pre-TCRs. If pre-TCR signaling indeed depends on nanoclusters, this could provide new therapeutic targets for the treatment of T cell acute lymphoblastic leukemia (T-ALL). TCR nanocluster integrity is regulated by specific membrane lipids (7, 9, 43, 44) and recent work on mature T cells in preclinical models of cancer immunotherapy has shown that manipulation of membrane cholesterol content in tumor-specific T cells can regulate their antitumor response (45). T-ALLs depend on pre-TCR signaling for their maintenance (46–48) and interference with pre-TCR nanoclusters could therefore be a relevant therapeutic approach with druggable targets.

Our findings make clear that  $\beta$ -selection permits maturation of DN thymocytes with a range of pre-TCR-dependent signaling capabilities, and this likely has consequences for the final TCR repertoire if reduced signaling capacity is maintained during the TCR signaling-dependent differentiation steps. In the context of the L19A mutation it would be expected that the reduced signaling capacity is maintained in the DP thymocytes,

**Table 1.** Diversity of WT and L19A TCR $\beta$  repertoires

	WT, mean $\pm$ SD	L19A, mean $\pm$ SD	Statistics
FSC <sup>hi</sup> CD69 <sup>-</sup> DP cells, no.	1.4 $\pm$ 0.8 $\times$ 10 <sup>5</sup> ( $n$ = 5)	0.4 $\pm$ 0.3 $\times$ 10 <sup>5</sup> ( $n$ = 5)	$P$ = 0.032 (Mann–Whitney $U$ )
In-frame reads, no.	8.4 $\pm$ 2.0 $\times$ 10 <sup>5</sup> ( $n$ = 5)	4.3 $\pm$ 1.4 $\times$ 10 <sup>5</sup> ( $n$ = 5)	$P$ = 0.016 (Mann–Whitney $U$ )
Diversity richness, $^0D$	7.6 $\pm$ 4.5 $\times$ 10 <sup>4</sup> ( $n$ = 5)	2.3 $\pm$ 1.5 $\times$ 10 <sup>4</sup> ( $n$ = 5)	$P$ = 0.032 (Mann–Whitney $U$ )
Estimated richness	7.9 $\pm$ 4.7 $\times$ 10 <sup>4</sup> ( $n$ = 5)	2.4 $\pm$ 1.5 $\times$ 10 <sup>4</sup> ( $n$ = 5)	$P$ = 0.032 (Mann–Whitney $U$ )
CD25 <sup>hi</sup> CD44 <sup>-</sup> DN cells, no.	8.6 $\pm$ 5.2 $\times$ 10 <sup>4</sup> ( $n$ = 4)	8.2 $\pm$ 1.9 $\times$ 10 <sup>4</sup> ( $n$ = 2)	$P$ = 0.800 (Mann–Whitney $U$ )
In-frame reads, no.	1.3 $\pm$ 1.4 $\times$ 10 <sup>5</sup> ( $n$ = 4)	3.6 $\pm$ 0.3 $\times$ 10 <sup>5</sup> ( $n$ = 2)	$P$ = 0.133 (Mann–Whitney $U$ )
Diversity richness, $^0D$	1.1 $\pm$ 0.9 $\times$ 10 <sup>4</sup> ( $n$ = 4)	1.4 $\pm$ 0.5 $\times$ 10 <sup>4</sup> ( $n$ = 2)	$P$ = 0.530 (Mann–Whitney $U$ )
Estimated richness	1.2 $\pm$ 0.9 $\times$ 10 <sup>4</sup> ( $n$ = 4)	1.4 $\pm$ 0.5 $\times$ 10 <sup>4</sup> ( $n$ = 2)	$P$ = 0.533 (Mann–Whitney $U$ )



as a recent report strongly suggests that nanoclustering of the TCR indeed occurs in these cells and is relevant for the outcome of positive and negative selection (44). Analysis of the 4SP-to-8SP ratio in WT and L19A thymi also provides support for this notion, with L19A thymi having a lower ratio than WT thymi (data underlying Fig. 1*A*;  $1.41 \pm 0.67$  vs.  $2.07 \pm 1.13$ ;  $P < 0.05$ , unpaired two-tailed Student's *t* test). Lineage choice is determined by TCR signaling strength at the CD8<sup>+</sup>CD4<sup>low</sup> stage of selection with a higher signaling capacity necessary for the CD4 lineage choice (49). It could be expected that TCRs with higher self-pMHC affinity would be allowed to mature, giving rise to a potentially autoreactive T cell repertoire. In a general context, mutation or allelic variation of components involved in signaling via the pre-TCR and/or variation in their expression level could be expected to have similar effects on pre-TCR signaling capacity of DN thymocytes, and promote the selection of higher-affinity clones upon differentiation to the DP stage.

While the increased cell death observed in L19A DN thymocytes would be expected to decrease TCR $\beta$  diversity at the early DP stage, this loss might be compensated by the reduced proliferation capacity of these cells, causing the niche to be filled by fewer descendants of each clone and thus allowing more room for additional clones. This is not the case, as both the number of clones in the large CD69<sup>+</sup> DP compartment is smaller in L19A mice (Fig. 4*B* and Table 1) and the numerical size of this compartment is significantly smaller in the L19A mice as compared with WT mice (SI Appendix, Fig. S5*D*). In a stochastic model for the relationship between diversity loss, proliferation, and death rate (SI Appendix, Text S2), we find that the loss of diversity scales with the ratio of rate of cell death over proliferation rate ("extinction probability"). Using as an approximation of changes in these rates the relative differences in percentages of proliferation and cell death (Fig. 2 *F* and *G*), the extinction probability of L19A thymocytes in transition from DN to early DP would be three- to fourfold higher than for WT thymocytes. Thus, reduced proliferation and increased propensity to die do not have opposing effects on repertoire diversity but both contribute to the reduction in diversity we observe.

The signaling capacity-dependent selection step we describe here does not appear to select particular molecular features of the TCR $\beta$  chain. We did not find changes in CDR3 length between DN3 and early DP thymocytes, or between WT and L19A DN3 and early DP thymocytes (SI Appendix, Fig. S5*E*), and an in-depth analysis of representation of VDJ combinations and the CDR3 amino acid sequences did not show clear patterns that were favored in either WT or L19A early DP thymocytes (SI Appendix, Fig. S5*F* and Dataset S1). These findings are compatible with the notion that the pre-TCR can signal independent of ligand engagement. They do not exclude the possibility that a noncanonical mode of pre-TCR-pMHC interaction takes place (31), taking into account that the reported variability in contacts between the TCR $\beta$  chain and the MHC class I molecule could preclude stringent selection of defined TCR $\beta$  features.

Our work shows that the intensity of pre-TCR signaling determines the diversity of the early TCR $\beta$  repertoire and proposes a mechanism for regulation of pre-TCR signaling strength by clustering. It also reveals that the pre-TCR imposes an unpredicted set point in the selection of the mature  $\alpha\beta$ TCR T cell repertoire.

## Materials and Methods

**Mice.** CD3 $\zeta$ WT-GFP and CD3 $\zeta$ L19A-GFP transgenic mouse lines were generated in the Centro Nacional de Biotecnología/Centro Biología Molecular Severo Ochoa (CNB/CBMSO) transgenesis facility. The previously described CD3 $\zeta$ WT-GFP and

CD3 $\zeta$ L19A-GFP cDNA sequences (8) were amplified with 5' and 3' flanking oligos containing an *Eco*RI and *Sal*I site, respectively, and cloned into the *Eco*RI and *Sal*I sites of the transgenic cassette vector p29 $\Delta$ 2 in which expression of the inserted DNA fragment is regulated by the hCD2 promoter and enhancer (14). Transgenic mice were obtained by injecting the promoter, transgene, and enhancer sequence-containing *Not*I fragment into C57BL/6JxSJL F1 one-cell-stage embryos and transplanting the embryos in pseudopregnant foster mothers. Two male founder mice for each transgenic construct (WT-F10, WT-F19, L19A-F13, and L19A-F23), initially identified via Southern blot using a GFP-specific probe, were selected and backcrossed once with C57BL/6J females to check for germ-line transmission and further backcrossed to a *Cd3e*<sup>tm1Lov</sup> knockout background (15). Relative copy numbers of the transgenes, as determined by qPCR analysis of genomic DNA, were three- to fivefold higher for the L19A lines as compared with the WT lines, which displayed similar copy numbers (SI Appendix, Fig. S1*E*). Mice backcrossed for two to five generations to the C57BL/6J background, homozygous for the *Cd3e*<sup>tm1Lov</sup> allele, and always carrying the transgene in hemizygosity were used for the experiments described in this manuscript. Knockin mice with a PxxP-to-AxxA double mutation in the PRS of CD3 $\epsilon$  were described previously (24). *Cd3e*<sup>tm1Lov</sup> knockout mice were obtained from the Jackson Laboratory (stock 004177) (19). Mice homozygous for the *Rag1*<sup>tm1Mom</sup> knockout allele (50) were kindly provided by César Cobaleda, CBMSO. Animals aged between 5 and 9 wk were used for all experiments. Mice were maintained under specific pathogen-free conditions in the animal facility of the CBMSO in accordance with applicable national and European guidelines. All animal procedures were approved by the ethics committees of the Consejo Superior de Investigaciones Científicas and the Comunidad Autónoma de Madrid (PRO-EX 68/14, PRO-EX 384/15, and PRO-EX 40.6/20).

**Antibodies and Reagents.** Antibodies used to detect the indicated mouse proteins were as follows: CD4-PerCP, -A647, -FITC (RM4-5), CD8-biotin, -PerCP, -647 (53-6.7), CD11b-biotin (M1/70), purified CD16/32 (2.4G2), CD19-biotin (1D3), CD25-PerCP, -APC, -PE (3C7), Gr1-biotin (RB6-8C5), and CD44-BV421, -PE, and -APC (IM7); TCR $\beta$ -APC, -PE, and -BV421 (H57-597); CD3 $\epsilon$ -PerCP, -APC, -PE, and -biotin (2C11), NK1.1-biotin (PK136), purified pT $\alpha$  (2F5), CD3 $\gamma\epsilon$ -APC (17A2), TCR $\gamma\delta$ -biotin (GL3), and pZAP70(Y319)-A674, obtained from BD Biosciences; and F4/80-biotin (BM8), CD98-PE (RL388), CD8-BV421 (53-6.7), and CD71-PE (R71217), all from eBioscience. Annexin V-PE, 7AAD, and the APC-labeled anti-BrdU mAb (3D4) were purchased from BD Biosciences. The APA1/1 mAb, which recognizes a conformational epitope of CD3 $\epsilon$ , and its use as a probe for the conformational change of the TCR have been described previously (22). Where necessary, secondary antibodies (anti-rabbit A647 and anti-mouse A647 from Thermo Fisher) or fluorescent probes (streptavidin-PerCP and -APC from BD Biosciences, streptavidin-PE from Invitrogen, and streptavidin-BV421 from BioLegend) were used.

**Flow Cytometry.** Thymi were homogenized with 40- $\mu$ m strainers and washed in phosphate-buffered saline (PBS) containing 1% bovine serum albumin (BSA). Single-cell suspensions were counted with a Scepter 2.0 cell counter and incubated with conjugated antibodies for 30 min at 4 °C after blocking Fc receptors using an anti-CD16/32 antibody. For intracellular staining, the Cytofix/Cytoperm Kit (BD Biosciences, 554714) was used according to provided instructions with incubation times for primary antibodies ranging from 30 min to overnight. For detection of apoptotic cells, an Annexin V Kit (BD Biosciences, 560930) was used following the provided protocol. For detection of proliferation of primary thymocytes in vivo, mice were injected intraperitoneally with 150  $\mu$ L of a BrdU solution (10 mg/mL). After 2 h, mice were killed and thymi were collected. Transmembrane proteins of thymocytes were labeled followed by fixation, permeabilization, DNase treatment, and anti-BrdU staining using a BrdU Flow Kit (BD Biosciences, 552598). Labeled cells were washed in PBS + 1% BSA and acquired on a FACS-Canto II (BD Biosciences). Data were recorded in a low-flow-rate mode to ensure a good resolution of the labeling. Analyses were performed using FlowJo software (BD Biosciences).

**TIRF Microscopy.** Pooled thymocyte suspensions from two or three WT or L19A mice were obtained and Lin<sup>+</sup> thymocytes were negatively selected using Ly6c, F4/80, CD11b, CD11c, CD19, B220, NK1.1, CD4, and CD8-specific antibodies and subsequently sheep anti-rat Dynabeads (Invitrogen, 11035). A second round of selection using a FACS Aria Fusion cell sorter was performed on

Lin<sup>−</sup> thymocytes to obtain DN CD44<sup>−</sup> thymocytes (DN3 + DN4 populations) that express GFP levels under 10<sup>3</sup> relative fluorescence units. This latter selection criterion, excluding the ~1% brightest DN cells, guaranteed that we could detect individual particles at the cell surface using the TIRF setting. Sorted DN CD44<sup>−</sup> thymocytes were left to recover in RPMI medium containing 5% fetal bovine serum for at least 2 h. Thirty minutes before TIRF microscopy analysis, thymocytes were seeded on microscopy plates pretreated with fibronectin (10 µg/mL, 60 min, 37 °C). Experiments were performed using a TIRF microscope (Leica, AM TIRF inverted) equipped with an electron-multiplying charge-coupled device camera (Andor, DU 885-CSO-10-VP), 100× oil-immersion objective (Leica, HCX PL APO 100×/1.46 numerical aperture), and 488-nm diode laser. The microscope was equipped with incubator and temperature control units; experiments were performed at 37 °C with 5% CO<sub>2</sub>. To minimize photobleaching effects before image acquisition, cells were located and focused using the bright field, and a fine focus adjustment in TIRF mode was made at 5% laser power, an intensity insufficient for single-particle detection that ensures negligible photobleaching. Image sequences of individual particles (500 frames) were acquired at 49% laser power with a frame rate of 10 Hz. The penetration depth of the evanescent field used was 90 nm. For the analysis, particles were detected and tracked using previously described algorithms [U-Track2 (51)] implemented in MATLAB. The intensity value for each particle was calculated by subtracting in each frame the background intensity from the particle intensity. In addition, to minimize photon fluctuations within a given frame, the particle intensity was represented as the average value (background-subtracted) obtained over the first 20 frames. For the short-time-lag diffusion coefficient ( $D_{1-4}$ ), only tracks longer than 50 frames were used for further analysis; particles that merged or split were excluded. Individual trajectories were used to generate mean-square-displacement (MSD) plots that were required to extract the  $D_{1-4}$  using the equation:  $MSD = 4D_{1-4}t + \Delta 0$ , where  $\Delta 0$  is the MSD offset at zero time lag. Additional details can be found in ref. S2.

**Analysis of TCR $\beta$  Repertoire.** DN3a (CD4<sup>−</sup>CD8<sup>−</sup>CD25<sup>+</sup>CD44<sup>−</sup>) and blasting DP (CD4<sup>+</sup>CD8<sup>+</sup>CD69<sup>−</sup>FCS<sup>hi</sup>) thymocytes of WT and L19A 5- to 8-wk-old male mice were purified by sorting. Messenger RNA was extracted from purified thymocytes using the RNeasy Micro Kit (QIAGEN, 74004). *Tcrb* amplicons were prepared using a 5' RACE-based protocol with the SMARTer Mouse TCR  $\alpha/\beta$  Profiling Kit (Takara, 634402) following the manufacturer's instructions. The *Tcrb* amplicons were purified using AmpureXP beads (Beckman Coulter, A63880) and sequenced in parallel via Illumina high-throughput sequencing on an Illumina MiSeq (2 × 300 nt) at the Centro Nacional de Análisis Genómico (CNAG-CRG), Barcelona, Spain. The quality of reads was assessed using FastQC (<https://www.bioinformatics.babraham.ac.uk/projects/fastqc/>). Raw sequencing reads were processed using MiXCR v3.0.8 software (53), allowing identification of CDR3 sequences, determination of V, D, and J genes, and assembly of clonotypes by CDR3 sequences. Taking into account the error rate of the sequencing methodology (54), a filter was applied to each library, grouping reads that differed in less than 3% of their CDR3 nucleotide sequence. Further analysis of clones was conducted using the iNEXT R package (29), in-house-written R scripts, and VDJtools v1.2.2 (55). The  $^qD$  was computed using a rarefaction/extrapolation algorithm and coverage was estimated using the same techniques.

**Statistical Analysis.** Statistical parameters including the exact value of  $n$  and the means  $\pm$  SEM are described in the text and figure legends. All results were

analyzed using GraphPad PRISM 7.0 (\* $P < 0.05$ , \*\* $P < 0.01$ , \*\*\* $P < 0.001$ , \*\*\*\* $P < 0.0001$ , or the exact  $P$  value). The TIRF microscopy lag diffusion coefficient ( $D_{1-4}$ ) and the mean fluorescence intensity (MFI) of single particles were analyzed using a two-tailed Mann-Whitney  $U$  nonparametric test. All other statistical analyses were performed using the parametric, two-tailed, and unpaired  $t$  test or the Mann-Whitney  $U$  test.

**Data Availability.** Raw sequencing data that underlie the analyses reported in Fig. 4 and *SI Appendix, Fig. S5* have been uploaded to the National Library of Medicine, National Center for Biotechnology Information (NLM NCBI) BioProject Sequence Read Archive and are freely available at <https://www.ncbi.nlm.nih.gov/bioproject/PRJNA609042> (56). cDNA amplicon data reported in this article can be accessed freely in the NLM NCBI BioProject Sequence Read Archive under accession no. PRJNA609042.

The mice generated in this study are available from the corresponding author with a completed Materials Transfer Agreement. Further information and requests for reagents may be directed to the corresponding author.

**ACKNOWLEDGMENTS.** We thank Cristina Prieto, Valentina Blanco, Tania Gomez, and the CBMSO flow cytometry service for excellent technical assistance; Belen Pintado and Veronica Dominguez from the CNB/CBMSO transgenic mouse facility for the generation of the CD3 $\zeta$ L19A-GFP and CD3 $\zeta$ WT-GFP mice; the CNAG-CRG for assistance with amplicon sequencing; Andreas Krüger for providing us with the SCB29 cell line; and Balbino Alarcon, Maria Luisa Toribio, and our laboratory members for their expert advice and critical analysis of this manuscript. E.R.B. was supported by a Formación de Personal Investigador (FPI) fellowship (BES-2014-068000, Subprograma Estatal de Formación del Programa Estatal de Promoción del Talento y su Empleabilidad, en el Marco del Plan Estatal de Investigación Científica y Técnica y de Innovación 2013 to 2016) and a European Molecular Biology Organization Short-Term Fellowship (7272). This work was supported by Spanish Ministry of Economy and Competitiveness (MINECO) Grants SAF2013-47975-R and SAF2016-76394-R and Grant PID2019-104703GB-I00/AEI/10.13039/501100011033 from the Spanish Ministry of Science and Innovation (MICINN) (to H.M.v.S.) and FIS2016-78883-C2-2-P (to M.C.). W.W.S. was supported by the German Research Foundation (DFG) through BIOS-EXC294 and CIBSS-EXC2189, SFB854 (B19), FOR2799 (SCHA976/8-1), and SFB1381 (A9). The Centre for Genomic Regulation acknowledges support of the Spanish Ministry of Economy and Competitiveness, "Centro de Excelencia Severo Ochoa," and the Centres de Recerca de Catalunya Program/Generalitat de Catalunya. The Centro Biología Molecular Severo Ochoa has been supported by the Fundación Ramón Areces.

Author affiliations: <sup>a</sup>Immune System Development and Function Unit, Centro Biología Molecular Severo Ochoa, Consejo Superior de Investigaciones Científicas/Universidad Autónoma de Madrid (CSIC/UAM), 28049 Madrid, Spain; <sup>b</sup>Department of Immunology and Oncology, Centro Nacional de Biotecnología, CSIC, 28049 Madrid, Spain; <sup>c</sup>Centre for Genomic Regulation, The Barcelona Institute of Science and Technology, 08003 Barcelona, Spain; <sup>d</sup>Department of Experimental and Health Sciences, Universitat Pompeu Fabra, 08002 Barcelona, Spain; <sup>e</sup>BIOS Centre for Biological Signalling Studies, University of Freiburg, 79104 Freiburg, Germany; <sup>f</sup>Centre for Integrative Biological Signalling Studies, University of Freiburg, 79104 Freiburg, Germany; <sup>g</sup>Department of Immunology, Faculty of Biology, University of Freiburg, 79104 Freiburg, Germany; <sup>h</sup>Centre for Chronic Immunodeficiency, University Clinics and University of Freiburg, 79110 Freiburg, Germany; <sup>i</sup>Grupo Interdisciplinar de Sistemas Complejos, Escuela Técnica Superior de Ingeniería, Universidad Pontificia Comillas de Madrid, 28015 Madrid, Spain; and <sup>j</sup>Servicio de Bioinformática, Centro Biología Molecular Severo Ochoa, CSIC/UAM, 28049 Madrid, Spain

1. M. Corr *et al.*, T cell receptor-MHC class I peptide interactions: Affinity, kinetics, and specificity. *Science* **265**, 946–949 (1994).
2. K. Matsui, J. J. Boniface, P. Steffner, P. A. Reay, M. M. Davis, Kinetics of T-cell receptor binding to peptide/I-Ek complexes: Correlation of the dissociation rate with T-cell responsiveness. *Proc. Natl. Acad. Sci. U.S.A.* **91**, 12862–12866 (1994).
3. J. B. Huppa *et al.*, TCR-peptide-MHC interactions in situ show accelerated kinetics and increased affinity. *Nature* **463**, 963–967 (2010).
4. S. Demotz, H. M. Grey, A. Sette, The minimal number of class II MHC-antigen complexes needed for T cell activation. *Science* **249**, 1028–1030 (1990).
5. C. V. Harding, E. R. Unanue, Quantitation of antigen-presenting cell MHC class II/peptide complexes necessary for T-cell stimulation. *Nature* **346**, 574–576 (1990).
6. D. J. Irvine, M. A. Purkhoo, M. Krosgaard, M. M. Davis, Direct observation of ligand recognition by T cells. *Nature* **419**, 845–849 (2002).
7. W. W. Schamel *et al.*, Coexistence of multivalent and monovalent TCRs explains high sensitivity and wide range of response. *J. Exp. Med.* **202**, 493–503 (2005).
8. R. Kumar *et al.*, Increased sensitivity of antigen-experienced T cells through the enrichment of oligomeric T cell receptor complexes. *Immunity* **35**, 375–387 (2011).
9. A. Martín-Leal *et al.*, CCR5 deficiency impairs CD4<sup>+</sup> T-cell memory responses and antigenic sensitivity through increased ceramide synthesis. *EMBO J.* **39**, e104749 (2020).
10. M. Castro *et al.*, Receptor pre-clustering and T cell responses: Insights into molecular mechanisms. *Front. Immunol.* **5**, 132 (2014).
11. K. A. Hogquist, S. C. Jameson, The self-obsession of T cells: How TCR signaling thresholds affect fate 'decisions' and effector function. *Nat. Immunol.* **15**, 815–823 (2014).
12. T. Nakayama, M. Yamashita, The TCR-mediated signaling pathways that control the direction of helper T cell differentiation. *Semin. Immunol.* **22**, 303–309 (2010).
13. M. Ciofani, J. C. Zúñiga-Pflücker, Determining  $\gamma\delta$  versus  $\alpha\beta$  T cell development. *Nat. Rev. Immunol.* **10**, 657–663 (2010).
14. D. R. Greaves, F. D. Wilson, G. Lang, D. Kioussis, Human CD2 3'-flanking sequences confer high-level, T cell-specific, position-independent gene expression in transgenic mice. *Cell* **56**, 979–986 (1989).
15. P. E. Love *et al.*, T cell development in mice that lack the zeta chain of the T cell antigen receptor complex. *Science* **261**, 918–921 (1993).
16. D. I. Godfrey, J. Kennedy, T. Suda, A. Zlotnik, A developmental pathway involving four phenotypically and functionally distinct subsets of CD3<sup>+</sup>CD4<sup>−</sup>CD8<sup>−</sup> triple-negative adult mouse thymocytes defined by CD44 and CD25 expression. *J. Immunol.* **150**, 4244–4252 (1993).



17. M. Groettrup *et al.*, A novel disulfide-linked heterodimer on pre-T cells consists of the T cell receptor beta chain and a 33 kd glycoprotein. *Cell* **75**, 283–294 (1993).
18. E. S. Hoffman *et al.*, Productive T-cell receptor beta-chain gene rearrangement: Coincident regulation of cell cycle and clonality during development in vivo. *Genes Dev.* **10**, 948–962 (1996).
19. J. B. DeJarnette *et al.*, Specific requirement for CD3epsilon in T cell development. *Proc. Natl. Acad. Sci. U.S.A.* **95**, 14909–14914 (1998).
20. M. Groettrup, A. Baron, G. Griffiths, R. Palacios, H. von Boehmer, T cell receptor (TCR) beta chain homodimers on the surface of immature but not mature alpha, gamma, delta chain deficient T cell lines. *EMBO J.* **11**, 2735–2745 (1992).
21. H. von Boehmer, Unique features of the pre-T-cell receptor alpha-chain: Not just a surrogate. *Nat. Rev. Immunol.* **5**, 571–577 (2005).
22. R. M. Risueño, D. Gil, E. Fernández, F. Sánchez-Madrid, B. Alarcón, Ligand-induced conformational change in the T-cell receptor associated with productive immune synapses. *Blood* **106**, 601–608 (2005).
23. R. Blanco, A. Borroto, W. Schamel, P. Pereira, B. Alarcon, Conformational changes in the T cell receptor differentially determine T cell subset development in mice. *Sci. Signal.* **7**, ra115 (2014).
24. A. Borroto *et al.*, Nck recruitment to the TCR required for ZAP70 activation during thymic development. *J. Immunol.* **190**, 1103–1112 (2013).
25. A. Borroto, A. Mallabiarrena, J. P. Albar, C. Martínez-A, B. Alarcón, Characterization of the region involved in CD3 pairwise interactions within the T cell receptor complex. *J. Biol. Chem.* **273**, 12807–12816 (1998).
26. A. Würch, J. Biro, I. Falk, H. Mossmann, K. Eichmann, Reduced generation but efficient TCR beta-chain selection of CD4<sup>+</sup>8<sup>+</sup> double-positive thymocytes in mice with compromised CD3 complex signaling. *J. Immunol.* **162**, 2741–2747 (1999).
27. I. Aifantis, J. Feinberg, H. J. Fehling, J. P. Di Santo, H. von Boehmer, Early T cell receptor  $\beta$  gene expression is regulated by the pre-T cell receptor-CD3 complex. *J. Exp. Med.* **190**, 141–144 (1999).
28. S. Yamasaki, T. Saito, Molecular basis for pre-TCR-mediated autonomous signaling. *Trends Immunol.* **28**, 39–43 (2007).
29. A. Chao *et al.*, Rarefaction and extrapolation with Hill numbers: A framework for sampling and estimation in species diversity studies. *Ecol. Monogr.* **84**, 45–67 (2014).
30. N. Martínez-Martín *et al.*, Cooperativity between T cell receptor complexes revealed by conformational mutants of CD3epsilon. *Sci. Signal.* **2**, ra43 (2009).
31. X. Li *et al.*, Pre-T cell receptors topologically sample self-ligands during thymocyte  $\beta$ -selection. *Science* **371**, 181–185 (2021).
32. D. Gil, W. W. Schamel, M. Montoya, F. Sánchez-Madrid, B. Alarcón, Recruitment of Nck by CD3 epsilon reveals a ligand-induced conformational change essential for T cell receptor signaling and synapse formation. *Cell* **109**, 901–912 (2002).
33. Y. Wang *et al.*, A conserved CXXC motif in CD3epsilon is critical for T cell development and TCR signaling. *PLoS Biol.* **7**, e1000253 (2009).
34. J. F. Brodeur, S. Li, M. da Silva Martins, L. Larose, V. P. Dave, Critical and multiple roles for the CD3epsilon intracytoplasmic tail in double negative to double positive thymocyte differentiation. *J. Immunol.* **182**, 4844–4853 (2009).
35. C. Xu *et al.*, Regulation of T cell receptor activation by dynamic membrane binding of the CD3epsilon cytoplasmic tyrosine-based motif. *Cell* **135**, 702–713 (2008).
36. E. Gagnon, D. A. Schubert, S. Gordo, H. H. Chu, K. W. Wucherpfennig, Local changes in lipid environment of TCR microclusters regulate membrane binding by the CD3 $\epsilon$  cytoplasmic domain. *J. Exp. Med.* **209**, 2423–2439 (2012).
37. S. Minguet, M. Swamy, B. Alarcón, I. F. Luescher, W. W. Schamel, Full activation of the T cell receptor requires both clustering and conformational changes at CD3. *Immunity* **26**, 43–54 (2007).
38. F. A. Hartl *et al.*, Noncanonical binding of Lck to CD3 $\epsilon$  promotes TCR signaling and CAR function. *Nat. Immunol.* **21**, 902–913 (2020).
39. M. Swamy *et al.*, A cholesterol-based allosteric model of T cell receptor phosphorylation. *Immunity* **44**, 1091–1101 (2016).
40. N. Martín-Blanco *et al.*, A window of opportunity for cooperativity in the T cell receptor. *Nat. Commun.* **9**, 2618 (2018).
41. S. Yamasaki *et al.*, Mechanistic basis of pre-T cell receptor-mediated autonomous signaling critical for thymocyte development. *Nat. Immunol.* **7**, 67–75 (2006).
42. S. S. Pang *et al.*, The structural basis for autonomous dimerization of the pre-T-cell antigen receptor. *Nature* **467**, 844–848 (2010).
43. E. Molnár *et al.*, Cholesterol and sphingomyelin drive ligand-independent T-cell antigen receptor nanoclustering. *J. Biol. Chem.* **287**, 42664–42674 (2012).
44. F. Wang, K. Beck-García, C. Zorzin, W. W. Schamel, M. M. Davis, Inhibition of T cell receptor signaling by cholesterol sulfate, a naturally occurring derivative of membrane cholesterol. *Nat. Immunol.* **17**, 844–850 (2016).
45. W. Yang *et al.*, Potentiating the antitumour response of CD8(+) T cells by modulating cholesterol metabolism. *Nature* **531**, 651–655 (2016).
46. D. Bellavia *et al.*, Combined expression of pTalpha and Notch3 in T cell leukemia identifies the requirement of preTCR for leukemogenesis. *Proc. Natl. Acad. Sci. U.S.A.* **99**, 3788–3793 (2002).
47. Y. Yashiro-Ohtani *et al.*, Pre-TCR signaling inactivates Notch1 transcription by antagonizing E2A. *Genes Dev.* **23**, 1665–1676 (2009).
48. M. Tremblay *et al.*, Modeling T-cell acute lymphoblastic leukemia induced by the SCL and LM01 oncogenes. *Genes Dev.* **24**, 1093–1105 (2010).
49. A. Singer, S. Adoro, J.-H. Park, Lineage fate and intense debate: Myths, models and mechanisms of CD4- versus CD8-lineage choice. *Nat. Rev. Immunol.* **8**, 788–801 (2008).
50. P. Mombaerts *et al.*, RAG-1-deficient mice have no mature B and T lymphocytes. *Cell* **68**, 869–877 (1992).
51. K. Jaqaman *et al.*, Robust single-particle tracking in live-cell time-lapse sequences. *Nat. Methods* **5**, 695–702 (2008).
52. L. Martínez-Muñoz *et al.*, Separating actin-dependent chemokine receptor nanoclustering from dimerization indicates a role for clustering in CXCR4 signaling and function. *Mol. Cell* **70**, 106–119.e10 (2018).
53. D. A. Bolotin *et al.*, MiXCR: Software for comprehensive adaptive immunity profiling. *Nat. Methods* **12**, 380–381 (2015).
54. J. Shendure, H. Ji, Next-generation DNA sequencing. *Nat. Biotechnol.* **26**, 1135–1145 (2008).
55. M. Shugay *et al.*, VDJtools: Unifying post-analysis of T cell receptor repertoires. *PLoS Comput. Biol.* **11**, e1004503 (2015).
56. E. R. Bovolenta *et al.*, TCRb repertoire of DN and large DP thymocytes from mice expressing a wild type or mutant CD3zeta chain. NLM NCBI BioProject Sequence Read Archive. <https://www.ncbi.nlm.nih.gov/bioproject/PRJNA609042>. Deposited 27 February 2020.